Eur. Phys. J. D **1**, 277–289 (1998)

**THE EUROPEAN PHYSICAL JOURNAL D**



# Quantum and semiclassical dynamics of differential optical collisions

F. Rebentrost[1], S. Klose[2], and J. Grosser[2]

[1] Max-Planck-Institut für Quantenoptik, 85740 Garching, Germany
[2] Institut für Atom- und Molekülphysik, Universität Hannover, 30167 Hannover, Germany

Received: 30 July 1997 / Received in final form: 5 November 1997 / Accepted: 8 January 1998

**Abstract.** We apply quantum and semiclassical theories to differential optical collisions $Na(3^2S_{1/2}) + Kr + \hbar\omega \rightarrow Na(3^2P_{1/2,3/2}) + Kr$. Our results provide a basis to analyze recent experiments in which for the first time optical collisions were investigated with angular resolution under crossed-beam conditions. A characteristic feature of the differential cross sections is the pronounced oscillatory structure due to interferences of different Condon paths. These Stueckelberg oscillations form an extremely sensitive probe of the collisional dynamics and of the molecular interactions. We demonstrate perspectives to determine geometric properties of the collision complex by excitation with polarized light. By final state analysis nonadiabatic (spin-orbit, rotational) interactions can be studied with complete control of the path. In summary it is shown that the method of differential detection of optical collisions opens a variety of new accesses to atomic and molecular subcollisions.

**PACS.** 32.70.-n Intensities and shapes of atomic spectral lines – 34.20.Cf Interatomic potentials and forces – 34.50.Rk Laser modified scattering and reactions

## 1 Introduction

In an optical collision a collision pair absorbs or emits a photon and undergoes a transition into another electronic state. Such processes are of interest both for the investigation of the detailed collision dynamics of atoms and molecules and for the collisional redistribution of light [1–6]. For the former aspect it is important to realize that in an optical collision the dynamics evolves on at least two electronic potentials of the quasimolecule. The extent to which the process probes a particular potential is controled by the laser frequency and the Franck-Condon principle. Since the optical transition thus normally occurs at well-defined distances of the collision partners, optical collisions provide an excellent method to study partial collisional events or equivalently the dynamics of collisions on a subcollisional time scale. The study of optical collisions is usually carried out with CW or pulsed light sources with ns time duration. At present, time-resolved experiments of collision processes have not been reported. However, the power of the time-domain approach is well documented by the experimental studies of photodissociation processes (half collisions) [7–10]. Optical collisions are often very sensitive to the long and intermediate range of the intermolecular potentials. This opens the possibility to test these potentials also in cases which are not readily accessible by the more conventional spectroscopic methods [3]. Optical collision experiments in cells and their theoretical analysis have lead to fundamental insights into the role of depolarization and nonadiabatic interactions [11–13]. In the context of collisional redistribution, finally, optical collisions play the role of the fundamental processes determining the redistribution of light by collisions (fluorescence, Rayleigh scattering, *etc.*)[4–6].

Recently remarkable experimental progress in optical collisions of atoms has been made along several routes. Detailed integral optical collision spectra have been obtained for a number of systems in cell experiments. Among them are the optical collisions of Hg [14] and Ba [15] with rare gas atoms. The results allow a systematic investigation of the effect of the atom-perturber interaction. Further, it has been possible to extend the regime of optical collisions to transitions starting from excited atoms. In this way also the higher lying potentials of alkali rare gas systems as well as the higher multiplicity cases (*e.g.* $\Delta$ states) become accessible [3]. Another promising development are multicolor experiments [16] in which a fraction of the collision is selected by the use of two photon energies. A large impact for the field is expected by the very recent success to monitor optical collisions under the conditions of a molecular beam experiment [17,18]. In the present work, we analyze the very detailed information which is contained in optical collision spectra measured with differential detection. The theoretical interpretation of optical collisions by the quantum approach provides an almost complete view of the detailed collision dynamics. It also is often used as a basis for comparison with other theoretical approaches, *e.g.* quasistatic, semiclassical, quantum mechanical lineshape

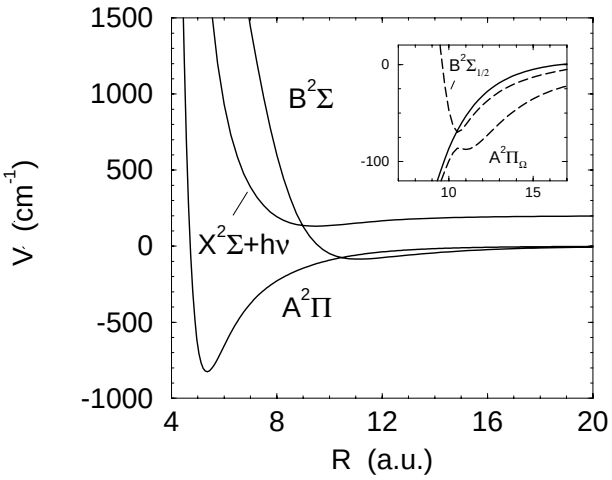


**Fig. 1.** Potential scheme for NaKr: Born-Oppenheimer (spin-free) potentials $X^2\Sigma$, $B^2\Sigma$ and $A^2\Pi$. The $X^2\Sigma$ potential is shifted by $\hbar\omega$ using a positive detuning $+200$ cm$^{-1}$. The inset shows the adiabatic excited state potentials, calculated by diagonalization of the sum of the spin-free potentials and the spin-orbit interaction. The dashed and solid curves in the inset represent the $\Omega = 1/2$ and $3/2$ states, respectively.

theories. The nonadiabatic character of optical collisions in real systems is most adequately treated by the quantum approach. On the other hand an at least semiquantitative understanding of the underlying mechanisms is often possible on simpler grounds, an example being the classical rotation model applied to depolarization in optical collisions [19]. A successful interpretation of optical collision spectra often however depends much on the availability of accurate information on the potentials and couplings.

In this work we consider the optical collision process

$$\mathrm{Na}(3^2\mathrm{S}_{1/2}) + \mathrm{Kr} + \hbar\omega \rightarrow \mathrm{Na}(3^2\mathrm{P}_{1/2,3/2}) + \mathrm{Kr}$$

for which differential cross sections have recently been measured for the first time under crossed beam conditions. The relevant potential curves are shown in Figure 1. By varying the laser detuning $\Delta\omega = \omega - \omega_{\mathrm{res}}$ on the blue side of the $\mathrm{Na}(3^2\mathrm{S}_{1/2} \rightarrow 3^2\mathrm{P}_{1/2})$ $\mathrm{D}_1$ resonance line ($\omega_{\mathrm{res}}/2\pi c = 16956.2$ cm$^{-1}$), we are sensitive to transitions from the ground $X^2\Sigma$ state to the repulsive, excited $B^2\Sigma$ state of NaKr. Similar for negative detuning the transition is to the attractive $A^2\Pi$ state. For positive detuning, experiment and theory show the occurence of pronounced, regular Stueckelberg oscillations in the differential cross sections. These result from the coherent superposition of paths in which the excitation occurs either for the in- or the out-going motion of the collision pair. Similar structures are quite frequent in atomic collisions, *e.g.* in differential cross sections for collisional electronic excitation, and in oscillatory lineshapes in Feshbach resonances [20, 21]. The Stueckelberg oscillations observed in differential optical collision spectra provide a wealth of detailed information on the collision dynamics that is absent in the more traditional experiments using cells.

In the following we outline the theoretical basis of the quantum and semiclassical approaches to differential optical collision cross sections (Sect. 2). Using the Stueckelberg patterns in the cross sections, we obtain an improved potential for the repulsive $B^2\Sigma$ state in NaKr (Sect. 3.1). In Section 3.2 we demonstrate how information on collision geometry at the instant of excitation is obtained with polarized light. The detailed properties of the collision products (alignment, orientation, population ratio of the fine-structure components) and their relation to nonadiabatic processes are considered in Section 3.3. Finally Section 4 summarizes the new possibilities to observe atomic and molecular collisions.

## 2 Quantum and semiclassical theories of optical collisions

### 2.1 Dressed-state coupled-channels theory

We consider optical collisions in alkali rare-gas systems

$$\mathrm{A}(^2\mathrm{S}_{J_0,m_0}) + \mathrm{X} + \hbar\omega \rightarrow \mathrm{A}(^2\mathrm{P}_{J,m_J}) + \mathrm{X} \qquad (1)$$

with $J_0 = 1/2$ for the ground and $J = 1/2$ or $3/2$ for the excited states. The quantum mechanical Hamilton operator is [22]

$$H = -\frac{\hbar^2}{2mR}\frac{\mathrm{d}^2}{\mathrm{d}R^2}R + \frac{\mathbf{l}^2}{2mR^2} + H_{\mathrm{el}} + V_{\mathrm{so}} + H_{\mathrm{ph}} + V_{\mathrm{rad}}. \quad (2)$$

The first terms describe the atomic collision system, $H_{\mathrm{ph}}$ represents the optical field, and $V_{\mathrm{rad}}$ is the interaction. The operator of the collision system is independent of the field and is a sum of the radial and centrifugal parts of the nuclear kinetic energy, the electronic (Coulomb) Hamiltonian $H_{\mathrm{el}}$ and the spin-orbit coupling $V_{\mathrm{so}}$. For $n_{\omega q}$ photons in a volume $V$ with polarization $q = 0, \pm 1$ one may write, in second-quantized form,

$$\begin{aligned} H_{\mathrm{ph}} &= \hbar\omega\, a_q^+ a_q = \hbar\omega\, n_{\omega q} \\ V_{\mathrm{rad}} &= \frac{e}{m_{\mathrm{e}}}\left(\frac{2\pi\hbar}{\omega V}\right)^{1/2}(a_q + a_q^+)p_q. \end{aligned} \qquad (3)$$

Here we consider only the dipole coupling to represent $V_{\mathrm{rad}}$. The dynamics of the collision system in the excited state manifold arising from the molecular $A^2\Pi$ and $B^2\Sigma$ states depends much on the $R$-dependent relative magnitude of the electrostatic interaction and the spin-orbit and rotational couplings expressed by the operators

$$V_{\mathrm{so}} = g\,\mathbf{L}\cdot\mathbf{S} \qquad (4)$$

and

$$H_{\mathrm{rot}} = \frac{\mathbf{l}^2}{2mR^2} = \frac{(\mathcal{J} - \mathbf{L} - \mathbf{S})^2}{2mR^2}\,. \qquad (5)$$

In the last equation $\mathcal{J}$ is the total angular momentum of the collision system formed by coupling the electronic

orbital momentum $\mathbf{L}$ and spin $\mathbf{S}$, (with $\mathbf{J} = \mathbf{L} + \mathbf{S}$) with the angular momentum of the internuclear motion $\mathbf{l}$. We expand the wave function in the form

$$\Psi = R^{-1} \sum_{\mathcal{J}MlJn} |\mathcal{J}MlJ> |n> u_{\mathcal{J}MlJn}(R) \qquad (6)$$

where $|\mathcal{J}MlJ>$ represents the electronic and the nuclear rotational motion, $|n>$ the state of the photon field, and the functions $u(R)$ describe the radial nuclear motion. After substitution into the Schrödinger equation with the Hamiltonian of equation (2) we obtain a set of coupled-channels equations for the radial functions

$$\left[\frac{\mathrm{d}^2}{\mathrm{d}R^2} + k^2(R) - \frac{l(l+1)}{R^2}\right] u_{\mathcal{J}MlJn}(R) = \frac{2m}{\hbar^2} \sum_{\mathcal{J}'M'l'J'n'} V^{\mathcal{J}MlJn}_{\mathcal{J}'M'l'J'n'} u_{\mathcal{J}'M'l'J'n'}(R). \qquad (7)$$

In equation (6) we used a Hund's coupling case $e$ basis for the molecular channel functions defined by

$$|\mathcal{J}MlJ> = \sum_{m_l m_J} C(Jl\mathcal{J}; m_J m_l M) Y_{lm_l}(\theta\phi) |Jm_J\beta> = \sum_{\Omega} (-)^{J-\Omega} C(J\mathcal{J}l; \Omega\bar{\Omega}0) |\mathcal{J}M\Omega J> \qquad (8)$$

where the functions $|\mathcal{J}M\Omega J>$,

$$|\mathcal{J}M\Omega J> = \left(\frac{2\mathcal{J}+1}{4\pi}\right)^{1/2} D^{\mathcal{J}*}_{M\Omega}(\phi\theta 0) |J\Omega>, \qquad (9)$$

are given in terms of the Wigner rotation matrices $D^{\mathcal{J}*}_{M\Omega}$ and electronic functions $|J\Omega>$ defined in the molecular frame. $M$ and $\Omega$ are the respective components of total angular momentum along the space- and molecule-fixed quantization axes. In the molecular frame $\Omega$ is also the projection of electronic angular momentum. To fully characterize the electronic and the resulting molecular channel functions additional quantum numbers $\beta$ may in general be necessary. The electronic functions $|J\Omega>$ in equation (9) are formed by coupling $\mathbf{L}$ and $\mathbf{S}$ in the $R$-dependent (spin-uncoupled) electronic Born-Oppenheimer functions exactly as in the case of free atoms

$$|J\Omega> = \sum_{\Lambda\Sigma} < L\, S\, \Lambda\, \Sigma | J\, \Omega > \; |\Lambda\Sigma\Omega> . \qquad (10)$$

In this way the electronic functions converge to atomic states at large separations. At finite $R$ the functions $|J\Omega>$ will however differ from the adiabatic electronic terms which would be obtained by diagonalizing $H_{\mathrm{el}}$ and $V_{\mathrm{so}}$ at each $R$. Here there is no practical advantage of the use of adiabatic electronic states since the transformation is $R$-dependent and leads to the unfavourable appearance of new radial coupling terms. In the representation of the molecular channel functions given by equations (8) and (9) the Hamiltonian matrix is completely determined in terms of electronic matrix elements in a molecular frame. Their explicit expressions are given in Appendix A.

In optical collisions the total angular momentum $\mathcal{J}$ of the molecular system is no longer conserved. In the weak-field case the absorption or emission of a photon with polarization $q$ leads to a change of $\mathcal{J}$ by either $\pm 1$ or 0, exactly as in the case of the $P$, $Q$ and $R$-branches in molecular spectroscopy

$$|\mathcal{J}' - \mathcal{J}| \leq 1; \quad M' = M \pm q. \qquad (11)$$

In the present case only the linear effect of the field is of interest since the photons are used to probe rather than to modify the dynamics of the collision. As a most important consequence of the linearity in the field it is then possible to completely separate the different branches $\mathcal{J} \to \mathcal{J}'$ and the $M$ dependence in the coupled-channels equations. This is seen from the appearance of the factor $C(\mathcal{J}1\mathcal{J}'; MqM')$ in equation (40) and leads to a considerable reduction of the computational effort [22].

For the final determination of the scattering matrices it is convenient to introduce a standard atomic dressed state basis discussed in Appendix B. In the linear case the asymptotic behavior of the wave function is chosen independent of the $M$ quantum number

$$u^{\mathcal{J}lJ}_{\mathcal{J}'l'J'}(R) \sim \delta_{\mathcal{J}\mathcal{J}'}\delta_{ll'}\delta_{JJ'}\sqrt{k_J}\, j_l(k_J R) - \frac{\sqrt{k_{J'}}}{2} T^{\mathcal{J}lJ}_{\mathcal{J}'l'J'}\, h_{l'}(k_{J'}R) \qquad (12)$$

and the Bessel functions $h_l$ and $j_l$ behave for $x \to \infty$ like

$$j_l(x) \xrightarrow[x\to\infty]{} \frac{\sin(x - l\pi/2)}{x}$$
$$h_l(x) \xrightarrow[x\to\infty]{} \frac{-i\, \exp[i(x - l\pi/2)]}{x}\,. \qquad (13)$$

This allows the determination of the scattering $T$ matrices at internuclear separations where the long-range centrifugal potential has not yet vanished as exploited in the well-known partial wave expansion techniques.

## 2.2 Scattering amplitudes; differential cross sections and multipoles

With the expression for the scattering amplitude

$$f^p_{J_0 m_0 \to Jm}(\hat{\mathbf{R}}, \mathbf{k}_0) = \frac{2\pi i}{k_0} \sum_{\mathcal{J}_0\mathcal{J}} \sum_{l_0 l m_{l_0} m_l} i^{l_0 - l} C(J_0 l_0 \mathcal{J}_0; m_0 m_{l_0} M_0) \times C(Jl\mathcal{J}; m m_l M) Y^*_{l_0 m_{l_0}}(\hat{\mathbf{k}}_0)\, Y_{lm_l}(\hat{\mathbf{R}}) T^{\mathcal{J}MlJn}_{\mathcal{J}_0 M_0 l_0 J_0 n_0} \qquad (14)$$

one obtains the differential optical collision cross sections

$$\frac{\mathrm{d}\sigma_{J_0 m_0 \to Jm}}{\mathrm{d}\Omega} = |f^p_{J_0 m_0 \to Jm}(\hat{\mathbf{R}}, \mathbf{k}_0)|^2. \qquad (15)$$

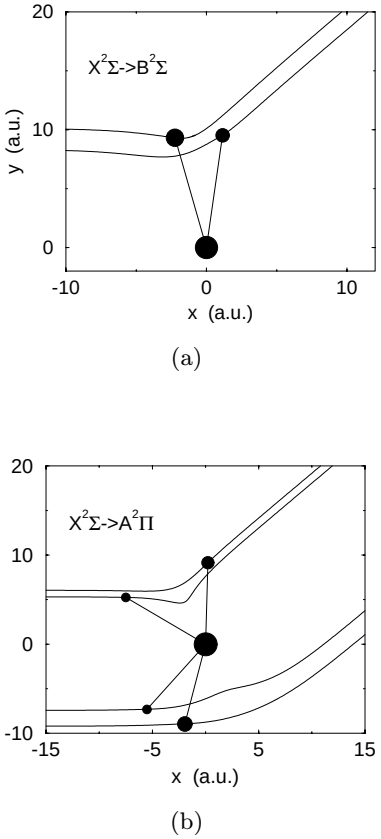


**Fig. 2.** Trajectories and Condon vectors for a scattering angle of 45°. The dots on the trajectories are the Condon transition points, their area is proportional to the semiclassical weight factor, see equation (21). a) positive detuning +200 $\mathrm{cm}^{-1}$, kinetic energy $\epsilon = 200$ $\mathrm{cm}^{-1}$; b) negative detuning −200 $\mathrm{cm}^{-1}$, $\epsilon = 800$ $\mathrm{cm}^{-1}$.

The full $T$ matrix required in equation (14) is obtained from the reduced $T$-matrix of equation (12) which is independent of $M_0$ and $M$ by

$$T^{\mathcal{J}MlJn}_{\mathcal{J}_0M_0l_0J_0n_0} = \delta_{n_0n+1}\, T^{\mathcal{J}lJ}_{\mathcal{J}_0l_0J_0} C(\mathcal{J}_0 1\mathcal{J}; M_0 pM)\, E_p. \quad (16)$$

The expression for the scattering amplitude simplifies by choosing a space-fixed coordinate system in which the $z$ axis coincides with the direction of $\hat{\mathbf{k}}_0$ (collision frame). Then

$$f^p_{J_0m_0\to Jm}(\hat{\mathbf{R}}) = \frac{2\pi i}{k_0}\sum_{\mathcal{J}_0\mathcal{J}}\sum_{l_0 l} i^{l_0-l}\sqrt{\frac{2l_0+1}{4\pi}}$$

$$\times C(J_0 l_0 \mathcal{J}_0; m_0 0 m_0)\, C(Jl\mathcal{J}; m m_l M) \quad (17)$$

$$\times Y_{lm_l}(\hat{\mathbf{R}}) T^{\mathcal{J}lJ}_{\mathcal{J}_0l_0J_0}\, C(\mathcal{J}_0 1\mathcal{J}; m_0 pM)\, \delta_{n_0n+1}\, E_p$$

using $Y^*_{l_0m_{l_0}}(\hat{\mathbf{0}}) = \delta_{m_{l_0}0}\sqrt{(2l_0+1)/4\pi}$. Of course $M = m_0 + p$ and $m_l = m_0 + p - m$ are given by the explicit components $m_0$, $m$ and $p$. In most cases the initial state is (spin-) unpolarized and the differential optical cross sections $\mathrm{d}\sigma_{J_0m_0\to Jm}/\mathrm{d}\Omega$ have to be averaged over the $m_0$ components of the initial state. Further, as long as the total intensities of the atomic $J$ levels are monitored independent of polarization effects, only the $m$-summed differential cross sections are of interest. They are

$$I_{J_0\to J}(\theta) = \frac{\mathrm{d}\sigma_{J_0\to J}}{\mathrm{d}\Omega} = \frac{1}{2J_0+1}\sum_{m,m_0}\frac{\mathrm{d}\sigma_{J_0m_0\to Jm}}{\mathrm{d}\Omega}\,. \quad (18)$$

The absolute scaling for the optical collision spectra follows from the linear dependence of all cross sections on the laser intensity $I_\omega = |E_p|^2 c/8\pi$. This is used here to define *e.g.* a differential cross section $\mathrm{d}q/\mathrm{d}\Omega$ for absorption of a photon per collision pair (units *e.g.* $\mathrm{A}^5$/srad) by equations (17) and (42)

$$n_\omega c\frac{\mathrm{d}q}{\mathrm{d}\Omega} = v\frac{\mathrm{d}\sigma}{\mathrm{d}\Omega} \quad (19)$$

and $v$ is the velocity of the collision.

The polarization of the scattered excited atoms is given by the multipoles of the atomic density matrix

$$\frac{\mathrm{d}\rho^{kq}_J}{\mathrm{d}\Omega} = \frac{1}{2J_0+1}\sum_{m_0,m}(-)^{k-J-m} C(JJk; -mm'q)$$
$$\times f^p_{J_0m_0\to Jm}(\hat{\mathbf{R}}) f^{p*}_{J_0m_0\to Jm'}(\hat{\mathbf{R}}). \quad (20)$$

For optical collisions in a cell experiment the collisions occur isotropically and coherences ($q \neq 0$) vanish. In the present situation the full multipole tensors contribute.

### 2.3 Semiclassical theory

In a semiclassical description of optical collisions, one exploits the close relation with the case of coupling between two diabatic states induced by an interaction $V_{12}(R)$. For the present situation the diabatic states are the "molecule + radiation field" states $V_1(R) = V_\mathrm{g}(R) + n\hbar\omega$ and $V_2(R) = V_\mathrm{e}(R) + (n-1)\hbar\omega$ as in Figure 1, and $V_{12}(R) = \mu(R)E/2$ is the dipole coupling. The optical transition occurs essentially at the crossing of the diabatic curves, *i.e.* at the Condon distance $R_\mathrm{c}$ for which $\hbar\omega = V_\mathrm{e}(R_\mathrm{c}) - V_\mathrm{g}(R_\mathrm{c})$. As before we will consider the case of weak coupling by the field and further neglect in this section the effects of spin-orbit and rotational interactions.

The classical trajectories for the optical collision switch at the Condon distance from the ground to the upper potential on either the in- or out-going motion. Examples of classical trajectories and Condon vectors, *i.e.* the internuclear vectors $\mathbf{R}_\mathrm{c}$ at the instant of the transition, are shown in Figure 2. In most cases there are more than one trajectory for a given scattering angle. In the insets of Figures 3 and 4 we also show examples of the classical deflection functions and the angles $\alpha_i$ of the Condon vectors with the collision frame $z$ axis.

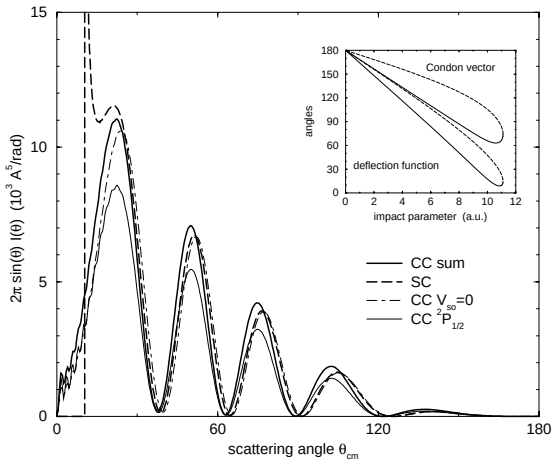


**Fig. 3.** Differential cross sections for excitation of $B^2\Sigma$ by quantum and semiclassical methods. Heavy solid line: Quantum result for summed $^2P_{1/2}$ and $^2P_{3/2}$ excitation, dashed line: the corresponding semiclassical result, thin solid line: quantum, only $^2P_{1/2}$ excitation, dot- dashed line: quantum sum $^2P_{1/2}$+$^2P_{3/2}$ calculated with $V_{so} = 0$. All data refer to a detuning of +200 cm$^{-1}$ and a kinetic energy of 200 cm$^{-1}$, the exciting light is polarized at 90° in the collision plane. The inset shows the corresponding classical deflection functions and the angular positions of the Condon vectors. Solid and dashed lines in the inset correspond to trajectories, for which the transition occurs during the out- or the ingoing motion, respectively.

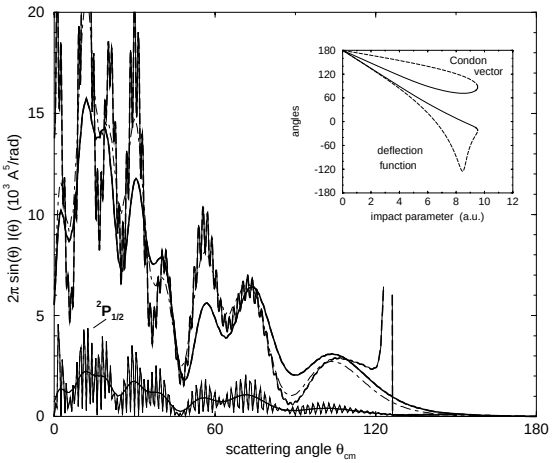


**Fig. 4.** Differential cross sections for excitation of $A^2\Pi$. The labeling is as in Figure 3. Detuning −100 cm$^{-1}$, kinetic energy 800 cm$^{-1}$, excitation with light polarized perpendicularly to the collision plane. The cross sections have been averaged over the rapid oscillations (angular resolution 2°). For $^2P_{1/2}$ also the cross section before averaging is shown. The inset gives the classical deflection functions and direction of the Condon vectors as in Figure 3.

The semiclassical expression for the differential cross section is in close analogy to the case of elastic scattering [20,18]

$$I(\theta) = \frac{1}{\sin\theta}\left|\sum_i \{p_i\, b_i/|\frac{\mathrm{d}\Theta}{\mathrm{d}b_i}|\}^{1/2} l_i \exp(i\phi_i)\right|^2 . \qquad (21)$$

The summation in equation (21) extends over all branches of the deflection function $\Theta$ contributing to a given scattering angle $\theta$. The dependence of $I(\theta)$ on the polarization of the exciting light enters through the factor $l = \mathbf{e}_\mu \cdot \mathbf{e}_\mathrm{p}$ with $\mathbf{e}_\mu$ and $\mathbf{e}_\mathrm{p}$ being unit vectors in the direction of the transition dipole and the polarization vector, respectively. For the case of a $\Sigma - \Sigma$ transition, $\mathbf{e}_\mu$ is along the internuclear axis, and hence $l_i = \cos(\alpha_i - \alpha_\mathrm{p})$ for linear polarization in the scattering plane where $\alpha_\mathrm{p}$ measures the direction of the field vector. Similarly we have $l_i = e^{\pm i\alpha_i}$ for right and left circular polarized light in the collision plane.

For the excitation probability $p_i$ at the Condon point we use the weak coupling limit of the Landau-Zener expression

$$p = \frac{2\pi V_{12}^2}{\hbar v_R |F|} \qquad (22)$$

where $v_R = v\{1 - b^2/R^2 - V_\mathrm{g}(R)/\epsilon\}^{1/2}$ and $F = \mathrm{d}V_1/\mathrm{d}R - \mathrm{d}V_2/\mathrm{d}R$ are the radial velocity and the slope of the difference potentials, respectively. All quantities in equation (22) are evaluated for $R = R_\mathrm{c}$, with $\epsilon = mv^2/2$ being the collision energy. The overall phase $\phi_i$ in equation (21) results from a stationary phase evaluation of the quantum mechanical scattering amplitude as

$$\phi_i = \Phi_i \pm (kb_i\theta - \pi/4) + \mathrm{sgn}(\frac{\mathrm{d}\Theta}{\mathrm{d}b_i})\pi/4 + \delta\phi \qquad (23)$$

and the JWKB phase shift $\Phi$ along the given trajectory is calculated from the deflection function $\Theta$ by

$$\Phi = k\int \Theta(b)\mathrm{d}b.$$

Accordingly the sign in front of the first bracket in equation (23) is fixed by the stationary phase condition $\Theta \pm \theta = 0 \bmod(2\pi)$ with $0 \le \theta \le \pi$. Finally an incremental phase $\delta\phi$ appears in equation (23) from the passage of the crossing region depending on the sign of $F$ and whether the transition occurs for the ingoing, $\delta\phi = \pi/4\ \mathrm{sgn}(F)$, or outgoing, $\delta\phi = -\pi/4\ \mathrm{sgn}(F)$, motion [20,23]. For the practical evaluation of equation (21) it is of advantage to avoid the singularity associated with the largest classically allowed impact parameter at which $v_{R_\mathrm{c}} = 0$ by replacing $\mathrm{d}\Theta/\mathrm{d}b$ in equation (21) by a corresponding derivative with respect to the radial velocity $v_{R_\mathrm{c}}$

$$I(\theta) = \frac{2\pi V_{12}^2 R_\mathrm{c}^2}{\hbar|F|v^2\sin\theta}\Big|\sum_i \left|\frac{\mathrm{d}\Theta}{\mathrm{d}v^i_{R_\mathrm{c}}}\right|^{-\frac{1}{2}} l_i\ \exp(i\phi_i)\Big|^2. \qquad (24)$$

As well known, other singularities, *e.g.* the ones associated with rainbows ($\mathrm{d}\Theta/\mathrm{d}b_i = 0$) for attractive potentials

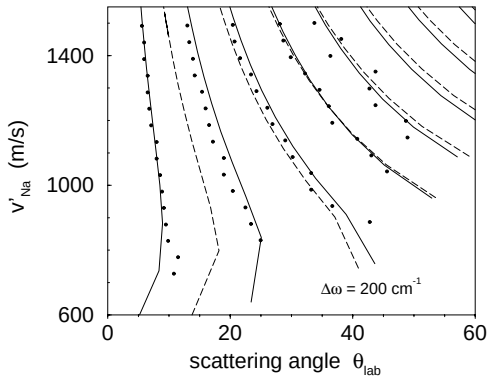


**Fig. 5.** Stueckelberg maxima in the experimental differential cross sections (dots) and optimization of the $B^2\Sigma$ potential by quantum theory: (- - -) using reference potential [28], (—) using optimized potential determined in reference [29]. This example is for a detuning of $+200$ cm$^{-1}$. For comparison with experiment the calculated data are transformed to laboratory scattering angle and final Na velocity.

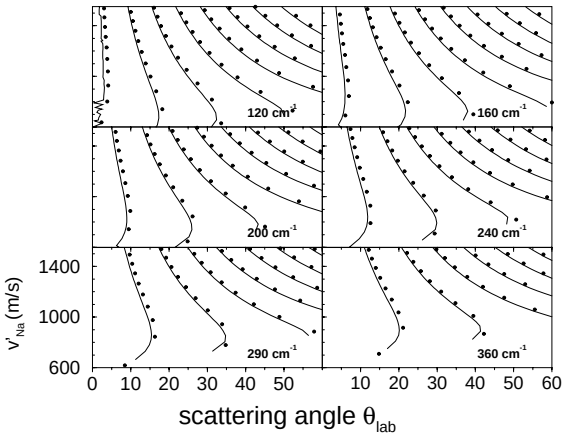


**Fig. 6.** Stueckelberg maxima in the differential cross sections. Comparison of quantum (—) and semiclassical (dots) results; positive detuning (excitation of $B^2\Sigma$). The data are transformed to laboratory scattering angles and final Na velocities as in Figure 5.

or satellites ($F = 0$) can in principle be treated by more sophisticated methods involving higher-order or uniform approximations. More important, in particular for a realistic modelling of the final-state distributions, is the implementation of nonadiabatic coupling effects in the upper state manifold. Rotational (Coriolis) coupling has been studied extensively in the past for simple S→P transitions on a semiclassical level [24,25]. Theory here has focused to great extent around the concept of a decoupling (locking) radius describing the effect of the transition from the molecular to the free-atom coupling of electronic angular momentum. A classical rotation model based on this concept has also been applied to depolarization in optical collisions to describe polarization effects [19,26]. At present we do not attempt to generalize our simple semiclassical approach that will be used together with the full quantum method which gives unambiguous results also in the more complex situations.

## 3 Results

### 3.1 Differential optical collision cross sections (DOCS)

In Figure 3 we show a typical differential cross section for optical collisions with excitation in the blue wing of the Na resonance. The agreement between the quantum and semiclassical results is almost perfect not considering of course the deviation at small angles and due to rainbow scattering. Since in our semiclassical calculation the branching into the fine-structure components is not treated at all, the comparison is made with the quantum results summed over the fine-structure components. The spin-orbit coupling becomes important for $R \geq 10$ a.u. (see Fig. 1). A small residual difference of $\sim 1°$ in the phase of the scattering amplitudes is mostly due to this coupling. The cause may well be a dynamic phase shift in the coupling region. The effects due to the change of the coupling case and of the potential asymptote are too small to account for this difference. This is further supported by calculations in which we set the spin-orbit interaction $V_{\rm so} = 0$ and the agreement between the quantum and semiclassical calculations was found to improve even more (Fig. 3). A similar high level of agreement between quantun and semiclassical results holds quite generally in all cases investigated here. Thus the semiclassical analysis forms an excellent basis for the physical interpretation of differential optical collisions.

The origin of the oscillations in the cross sections is then immediately clear from the semiclassical picture: the two signal contributions, as *e.g.* in Figure 2 for the case of blue detuning, interfere with usually different phase and weight factor in equation (21). The semiclassical calculations further provide a unique assignment of the order of the maxima, $\Delta\phi = \pm 2k\pi$, and minima, $\Delta\phi = \pm(2k+1)\pi$, $k = 0, 1, 2, ..$, in the differential cross sections.

In the red wing, we find a more complicated interference pattern, see Figure 4. This is expected by the classical theory. The $A^2\Pi$ potential is attractive and in general there are now four rather then two interfering contributions to the scattering amplitude, see Figure 2. Furthermore rapid oscillations occur due to the interference of attractive and repulsive trajectories (positive or negative $\Theta$). They should be observable only with extremely high angular resolution and disappear when some angular averaging is performed. Then, as seen in Figure 4, a more regular interference pattern appears and the quantum results are in complete agreement with the semiclassical analysis as far as the phases are concerned. Some deviations in the absolute magnitudes of the cross sections as well as in the contrast of the structures are attributed to the more complex excitation mechanism involving the two components of the $A^2\Pi$ state.

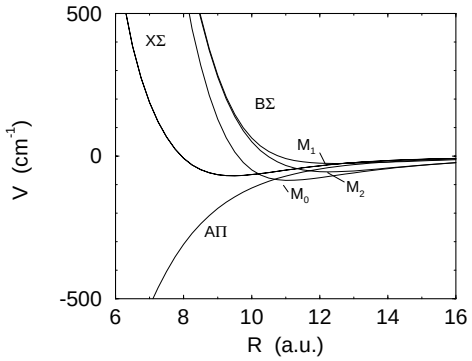


**Fig. 7.** Comparison of different results for the $B^2\Sigma$ (spin free) potential, showing an enlarged view of the nonadiabatic coupling region. $M_0$: model potential calculation [28]. $M_1$ and $M_2$: improved potentials both reproducing equally well the Stueckelberg patterns as in Figure 5. $M_2$ is used in the present calculations since it is in better agreement with measured fine-structure population ratios. The $X^2\Sigma$ and $A^2\Pi$ potentials are from reference [27].

The Stueckelberg oscillations in the DOCS are strongly dependent on the detailed intermolecular potentials involved. For the NaKr system only the $X^2\Sigma$ ground state and the $A^2\Pi$ terms have been characterized experimentally by spectroscopic methods [27]. Information on the repulsive $B^2\Sigma$ state potential cannot be obtained in this way and correspondingly the potential is known with much less accuracy. There are however model potential calculations by Düren *et al.* [28] which have been used here as reference potential. We determined an improved $B^2\Sigma_{1/2}$ potential such as to reproduce the observed maxima in the DOCS (Fig. 5). In the process of optimizing potential parameters the semiclassical approach is very effective. However all final results were confirmed by the quantum calculations, see Figure 6. More details on this procedure and an accuracy estimate of the final potential (see Fig. 7) are given in [29].

## 3.2 Optical collisions with polarized light and collision geometry

The reflection symmetry of the electronic wave function at the scattering plane is a constant of motion also for optical collisions. For the following it is therefore convenient to work with the scattering amplitudes defined for the cartesian rather than the spherical field components that were used in equation (17)

$$\begin{aligned} f^x &= \frac{-(f^1 - f^{-1})}{\sqrt{2}}; \\ f^y &= \frac{i(f^1 + f^{-1})}{\sqrt{2}}; \\ f^z &= f^0. \end{aligned} \tag{25}$$

Quite generally, the observedintensity then depends on the polarization of the exciting light according to ($i, j = x, y, z$)

$$I(\theta) = \mathrm{Re}\sum_{ij} f^{i*} f^j = \sum_{ij} A_{ij}(\theta)\, E_i E_j \tag{26}$$

where $A_{ij}$ is defined by equation (26) and is independent of the field amplitude. For the characteristic situation prevailing on the blue side ($\Delta\omega > 0$) of the NaKr optical collision spectrum, the interferences in the differential spectra arise by the superposition of only two paths. In this case the Stueckelberg patterns are very pronounced and can easily be used to obtain geometric information on the collision pair at the instant of excitation.

### 3.2.1 Initial alignment and average Condon vectors

We consider excitation by light polarized linearly in the scattering plane. By rotating the field vector in the plane until maximal scattering intensity occurs one determines the initial alignment angle $\alpha$ of the excited charge cloud at a given scattering angle. Intuitively this is equivalent to an average Condon vector. The observed intensity at each scattering angle depends on the angle $\alpha_\mathrm{p}$ of the electric field vector $\mathbf{E}_\mathrm{p}$ (measured from the collision plane $z$ axis) by

$$I(\theta, \alpha_\mathrm{p}) \;=\; |f^x(\theta)\sin\alpha_\mathrm{p} + f^z(\theta)\cos\alpha_\mathrm{p}|^2. \tag{27}$$

Figure 8 shows the polarization angle $\alpha_\mathrm{p} = \alpha^\mathrm{coh}$ at which maximal intensity is found according to equation (27). As function of the scattering angle one notices a continuous trend with strong variations superimposed around the minima in the differential cross sections. This behaviour is well understood and reproduced by the semiclassical analysis. Here the differential cross section for the situation prevailing for blue detuning is

$$\begin{aligned} I(\theta, \alpha_\mathrm{p}) =& |w_1^{1/2}\cos(\alpha_1 - \alpha_\mathrm{p})\exp(i\phi_1) \\ &+ w_2^{1/2}\cos(\alpha_2 - \alpha_\mathrm{p})\exp(i\phi_2)|^2. \end{aligned} \tag{28}$$

With this $\alpha^\mathrm{coh}$ is found to be (mod $\pi/2$)

$$\alpha^\mathrm{coh} = \bar{\alpha} + \frac{1}{2}\arctan\frac{(1-w)\sin(\alpha_2 - \alpha_1)}{(1+w)\cos(\alpha_2 - \alpha_1) + 2w^{1/2}\cos(\phi_2 - \phi_1)}\,. \tag{29}$$

Here $w = w_1/w_2$ is the relative weight of the two contributing trajectories, with $w_i = p_i b_i / \sin\theta |\mathrm{d}\Theta/\mathrm{d}b_i|$ as in equation (21), $\phi_i$ are the corresponding phases, and $\bar{\alpha} = (\alpha_1 + \alpha_2)/2$ is the arithmetic mean of the two Condon direction angles. As seen in the figure the quantum and semiclassical predictions agree very well again both in the structures due to the interference as well as in their respective magnitudes. A small difference in the relative phase has the same origin as discussed in Section 3.1. As

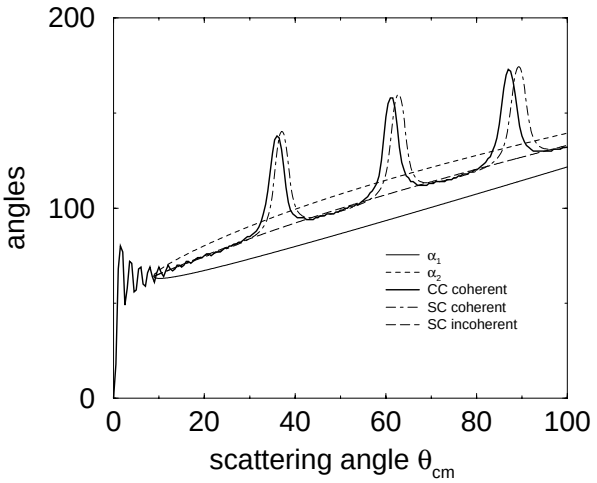


**Fig. 8.** Quantum and classical main axes directions of the initial alignment tensor leading to maximal intensity by excitation with linearly in-plane polarized light. Heavy solid line: Quantum result, dot-dashed: semiclassical coherent result, long-dashed: semiclassical incoherent average. The short dashed and solid lines show the angular positions of the two Condon vectors. The incoherent result represents the average direction of the Condon vectors. Detuning +200 $cm^{-1}$, kinetic energy 200 $cm^{-1}$.

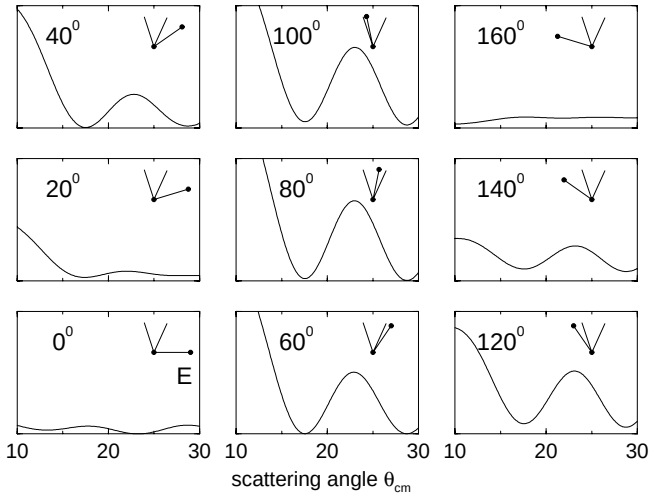


**Fig. 9.** Collision geometry and excitation by linear polarized light: Variation of the interference pattern with the direction of the polarization for positive detuning +200 $cm^{-1}$, kinetic energy 1000 $cm^{-1}$. The polarization is in the collision plane, the polarization angle relative to the initial velocity is indicated in the boxes. The insets show the Condon vectors, which are the same in all cases and the polarization vector. The oscillations disappear, when the polarization is at right angles to one of the Condon vectors, *e.g.* at 160°.

special cases we consider the initial alignment angle $\alpha$ at the maxmima and minima of the differential cross section

$$\alpha^{\mathrm{coh}} = \bar{\alpha} + \frac{1}{2}\arctan\frac{(1-w)\sin(\alpha_2-\alpha_1)}{(1+w)\cos(\alpha_2-\alpha_1) \pm 2w^{1/2}}\,. \tag{30}$$

From an analysis of equations (29) and (30) it follows that $\alpha$ lies generally in between the directions of the two separate Condon vectors. Near the interference minima an optimal signal is reached for a completely different direction. This arises formally from small values of the denominator $(1+w)\cos(\alpha_2-\alpha_1) - 2w^{1/2}$. In Figure 8 also the case of incoherent averaging the two Condon waves with

$$\alpha^{\mathrm{inc}} = \bar{\alpha} + \frac{1}{2}\arctan\{\frac{1-w}{1+w}\tan(\alpha_2-\alpha_1)\} \tag{31}$$

is given which apart from the region of the minima in the DOCS compares quite well with the quantum value of $\alpha$. The incoherent average further applies if the coherent average Condon vector is monitored with low angular resolution. One can also show that $\alpha^{\mathrm{inc}}$ is a weighted average of the two angles $\alpha_1$ and $\alpha_2$ according to

$$\alpha^{\mathrm{inc}} = q_1\alpha_1 + q_2\alpha_2 \tag{32}$$

with

$$\frac{q_1}{q_2} = \frac{\mathrm{arccot}[(w^{-1}+\cos 2(\alpha_2-\alpha_1))/\sin 2(\alpha_2-\alpha_1)]}{\mathrm{arccot}[(w+\cos 2(\alpha_2-\alpha_1))/\sin 2(\alpha_2-\alpha_1)]};$$
$$q_1+q_2=1. \tag{33}$$

In this way $\alpha^{\mathrm{inc}}$ is a direct measure of the average direction of the Condon vectors. Experimental results can be found in [30].

### 3.2.2 Separate Condon vectors

The determination of the directions of the two separate Condon vectors is possible as well. By choosing the polarization at right angle to one of the Condon vectors the Stueckelberg interference pattern is suppressed. Thus the angular positions of the single Condon vectors can be identified by looking at those polarization angles for which a minimal variation occurs in the differential cross sections (Fig. 9). This has also been realized experimentally [30].

Next we consider excitation of the collision pair by light which is circularly polarized in the collision plane. For the cases of right (+) and left (−) circular polarization the quantum differential cross section is

$$I(\theta,\pm) \;=\; |f^z(\theta) \pm i f^x(\theta)|^2. \tag{34}$$

The results of Figure 10 show a characteristic phase difference for the two orientations. The semiclassical analysis offers a simple explanation by

$$I(\theta,\pm) = |w_1^{1/2}\exp(\pm i\alpha_1)\exp(i\phi_1) + w_2^{1/2}\exp(\pm i\alpha_2)\exp(i\phi_2)|^2. \tag{35}$$

Thus the two signal contributions have to be superimposed with different phases for right and left circular polarization. The phase difference amounts to

$$\phi^+ - \phi^- = 2(\alpha_1-\alpha_2). \tag{36}$$

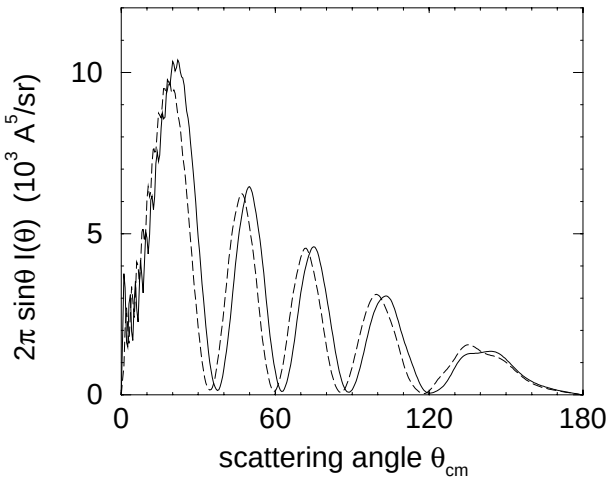


**Fig. 10.** The differential optical collision cross section for excitation with in-plane left (dashed) and right (solid line) circularly polarized light; Detuning +200 $cm^{-1}$, kinetic energy 200 $cm^{-1}$.

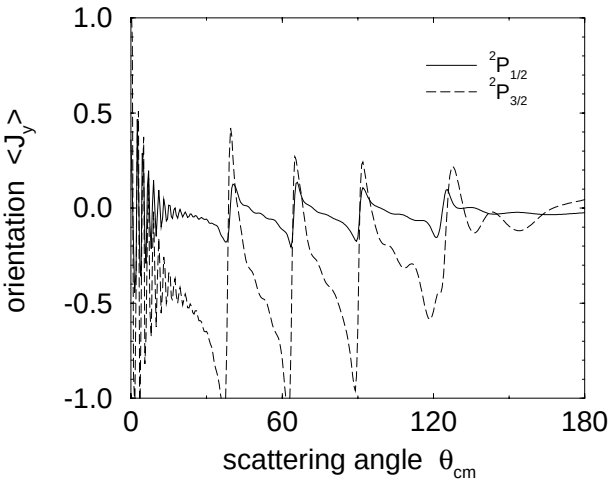


**Fig. 11.** Differentially resolved orbital orientation for the $^2P_{1/2}$ (dashed) and $^2P_{3/2}$ (solid line) components; Detuning +200 $cm^{-1}$, kinetic energy 200 $cm^{-1}$.

As demonstrated in [30] this opens the possibility to measure the angle between the Condon vectors. It is further seen from the semiclassical analysis that the Stueckelberg oscillations can be shifted to an arbitrary position by using an adequate elliptic polarization. As an example, for a linear polarization direction between the Condon vectors, the Stueckelberg maxima occur in the middle between the maxima for the two circular polarization cases. By choosing the linear polarization at right angles, the maxima and minima are interchanged.

Quite generally, methods as discussed in this section are capable, at least in principle, to determine the separate Condon vectors and their relative weights also in cases, when there are more than two Condon vectors.

### 3.3 Final state analysis: Orientation, alignment and fine-structure interactions

The final state of the alkali atom is characterized by the population ratio of the fine structure components and by its polarization properties, which are most readily expressed in terms of orientation and alignment.

#### 3.3.1 Orientation and alignment

For a situation with unpolarized atoms before the collision and with the electric vector in the collision plane, the final orientation tensor $T^1 \sim < \mathbf{J} >$ by reflection symmetry must point into the $y$ direction, *i.e.* at right angles to the scattering plane. A choice of the electric vector outside the scattering plane breaks the reflection symmetry and can lead to nonvanishing components $< J_x >$ and $< J_z >$. For excitation of a molecular $\Sigma$ state, only the in-plane component of the electric field is active. In this case $< J_x >=< J_z >= 0$, even when the field is out-of-plane.

The origin of orientation is the rotational coupling by the Coriolis operator $-l_y\, J_y/mR^2$ (see Eq. (5)), which mixes molecular terms with different $\Omega$ and decouples the electronic angular momentum from the internuclear axis at large distances. It leads already to a nonvanishing orientation if only a single classical trajectory contributes to the signal [25]. In addition, the coherent superposition of contributions from different trajectories in general results in a nonvanishing orientation, even when the single contributions do not possess an orientation. This depends strongly on the relative phase of the contributions, and an orientation with such an origin should be correlated to the Stueckelberg interference pattern.

In Figure 11, we show an example for the behaviour of the orientation in a differential optical collision. The fine-structure interaction seems to have a large effect on the orientation. One notices a much smaller $< J_y >$ value for the $^2P_{1/2}$ component than for the $^2P_{3/2}$ component. As a guideline one can compare with the ratio $< J_y >_{3/2} / < J_y >_{1/2}= 5/2$ following on general grounds in the limit of a sudden transition through the region where the fine-structure interaction operates. The same limit applies if the spin-orbit coupling is small with respect to Coulombic and rotational interactions. Note that in the $^2P_{1/2}$ case, rotational coupling is indeed less important, because the energy gap to the nearest state with $\Omega = 3/2$ value is comparatively large. Rotational coupling is expected to be much more effective between those two $\Omega = 1/2$ and $\Omega = 3/2$ components, which become degenerate when they asymptotically reach the $^2P_{3/2}$ state. For the case shown in Figure 11 we conclude from the vanishing of $< J_y >$ near the maxima of the differential cross section that the orientation observed at other angles is due only to the interference effect.

For excitation of a $\Pi$ state also the excitation process itself can break the planar reflection symmetry and thereby transfer orientation to the collision system if the

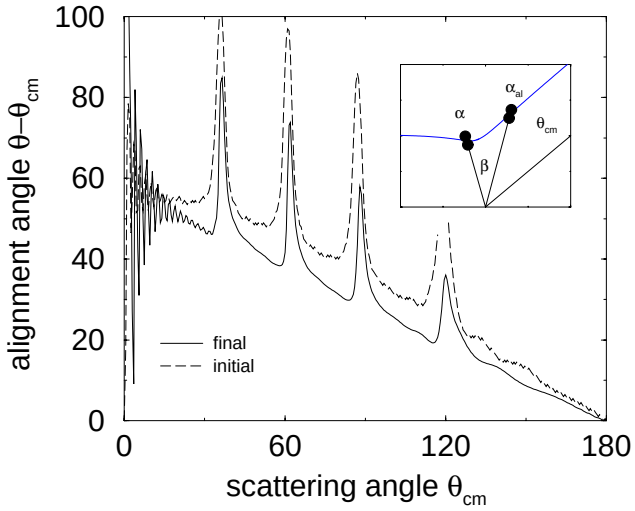


**Fig. 12.** Differentially resolved orbital alignment angle $\alpha_{al}$ (solid line) for the $^2P_{3/2}$ component; Detuning +200 cm$^{-1}$, kinetic energy 200 cm$^{-1}$. For comparison also the initial alignment angle $\alpha_{av}$ of Figure 8 is shown. The inset indicates the meaning of the angles and the trajectory schematically. The difference $\beta = \alpha_{al} - \alpha$ is an average rotation angle of the electronic orbital during the collision.

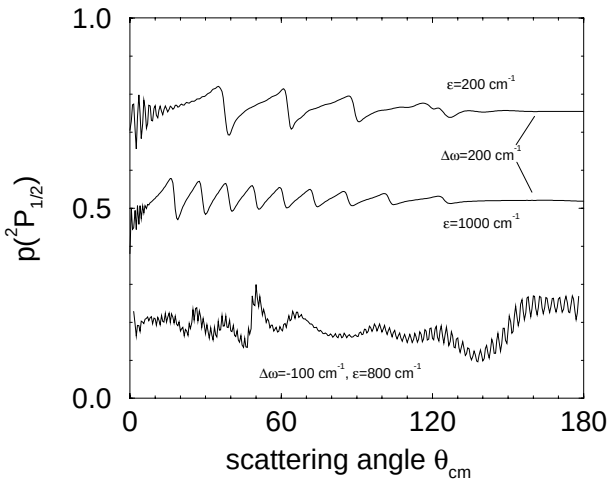


**Fig. 13.** Differentially resolved relative $^2P_{1/2}$ fraction of the total $^2P$ excitation. For negative detuning, an angular average with a resolution of 2° was performed.

light has components both in and perpendicular to the collision plane. This leads to a generally much larger orientation relative to excitation of a $\Sigma$ state. Such a situation arises always for isotropic collisions in cell experiments performed with circularly polarized light.

A nonzero value of the alignment tensor $T^2$ is possible only for the $^2P_{3/2}$ level. In cartesian coordinates, $T^2_{ij} \sim < \frac{1}{2}(J_iJ_j + J_jJ_i) - \frac{1}{3}\delta_{ij}J(J+1) >$ is characterized by its main axes. By reflection symmetry, two of the main axes are in the scattering plane. The direction of the major main axis defines the final alignment angle which characterizes the direction into which the Na($^2P_{3/2}$) wave function points after the collision. Comparing as in Figure 12 the average Condon vector (Sect. 3.2) and the final alignment angle gives an angle $\beta$, through which the wave function has been rotated on average between excitation and decoupling. In more detail the angle $\beta$ can also be obtained for the separated trajectories by the procedure of Section 3.2.2 to select a specific Condon vector. The rotation angle $\beta$ has a relatively small value, typically below 10°, which is consistent with calculations of the alignment tensor under thermally averaged isotropic conditions. The experimental results of Behmenburg and Ermers [13] require larger rotation angles leading to larger depolarization. It seems that the decoupling occurs too early with the present potentials. Since we are quite sure about the accuracy of the potential in the inner region, this indicates the necessity of some adjustment also of the long-range parts of the B$\Sigma$ and A$\Pi$ potentials.

### 3.3.2 Fine-structure ratios

In Figure 13, results for the relative excitation probabilities of the final $^2P_{1/2}$ and $^2P_{3/2}$ states are given for various detunings and collision energies. In all cases the data are characterized by an almost angle-independent average value on which stronger variations of the minima in the differential cross sections (Figs. 3 and 4) are superimposed. We conclude that the nonadiabatic transition probability on a selected trajectory is only weakly dependent upon the impact parameter. This is also supported by the partial wave analysis of the coupled-channels cross sections. The strong variations seen in Figure 13 are a consequence of a small phase shift difference in the partial differential cross sections for the $^2P_{1/2}$ and $^2P_{3/2}$ states. In practice structures likes this or in the corresponding polarization data, Figures 11 and 12, will be difficult to observe due to the low intensities near the Stueckelberg minima.

The excitation probabilities show a predominantly diabatic correlation between the molecular and the atomic channels: excitation of the upper B$^2\Sigma$ molecular state populates preferentially the lower $^2P_{1/2}$ atomic state. Correspondingly excitation of the lower A$^2\Pi$ molecular states mostly leads to the upper $^2P_{3/2}$ atomic states. This is a consequence of the intersection of the B$^2\Sigma$ and A$^2\Pi$ curves already shown in Figure 1. A Landau-Zener analysis of this crossing between the $\Omega = 1/2$ levels leads to large nonadiabatic transition probabilities of order 1, *i.e.* the system behaves in this region almost diabatically. The final populations will also depend on the second coupling region ($R \simeq 15$ a.u.) where the long-range $\Sigma - \Pi$ separation is again comparable to the fine-structure splitting $\Delta$ (17.2 cm$^{-1}$ for Na). Due to the presently unknown accuracy of the long-range parts of the potentials and also to the lack of experimental fine structure population ratios measured with the differential detection method,

we limit ourselves to a preliminary discussion. As seen in Figure 7, an adjustment of the long-range potential for the $B^2\Sigma$ state was performed resulting in the modification M2 in order to better reproduce the experimental $^2P_{1/2}/^2P_{3/2}$ ratios from gas cell experiments. For $\Delta\omega = 200$ cm$^{-1}$ the $^2P_{1/2}/^2P_{3/2}$ ratios measured by Behmenburg and Ermers [13] at $T = 440$ K are 2.5, while Havey *et al.* [31] report a value of 3.5 for 303 K. Our thermally averaged coupled-channels calculations give 2.2 and 2.8 for these temperatures while the single-energy value for a collision energy of 200 cm$^{-1}$ is about 3. A similar comparison in the red wing at $\Delta\omega = -100$ cm$^{-1}$ leads to values of 0.3-0.4 for the gas cell experiments and 0.3 in our calculations. We also note the trend to reach the sudden-impact limit, $^2P_{1/2}/^2P_{3/2}$=0.5, on both sides of the resonance line at higher collision energies.

The preceeding examples show that the final state analysis of differential optical collisions can be expected to form a very sensitive probe for the nonadiabatic coupling regions, and especially for the asymptotic parts of the excited molecular potentials.

## 4 Summary

The investigation of optical collisions under differential scattering conditions opens a variety of new methods for the observation of atomic collisions. The examples discussed in the preceding chapters represent only a few of them. More general categories of experiments can be considered along the following lines.

(1) *Determination and testing of interatomic potentials:* As illustrated by Figure 5 the method has already been successfully applied to the repulsive NaKr $B^2\Sigma$ potential curve [29]. This potential curve has been determined with an estimated accuracy of $\pm 25$ cm$^{-1}$, but a few cm$^{-1}$ appear within reach. Repulsive potentials are often not accessible by spectroscopic methods. Even when spectroscopic methods apply, the results frequently have an accuracy comparable to that of the methods discussed here. Attractive potentials show a much richer interference structure than repulsive ones, see Figure 4. Differential optical collision data are therefore expected to be considerably more sensitive to the potential curve for attractive than for repulsive potentials. For regions accessible by the Franck-Condon principle in an optical collision the new methods should be capable to compete with spectroscopic methods not only for repulsive but also for attractive potentials. For comparison spectroscopic experiments in many practical cases only probe rather limited regions of the internuclear distance, whereas differential optical collision data are sensitive to extended, in particular the long and intermediate $R$ ranges.

(2) *Observation of the geometric properties of the collision complex:* The direct observation of the geometric properties of a collision complex is presently a completely new and fascinating experimental tool, which in future will have many applications also to more complicated collisional systems, *e.g.* atom - molecule collisions. Investigations with atoms are valuable test cases, which help us to explore and to optimize the power of the new tool. Figure 9 demonstrates, how the directions of the two Condon vectors can be read out immediately from the differential cross sections. A refined analysis of the Stueckelberg pattern and its variation with the polarization will allow to determine more geometric details, *e.g.* the relative weight of the signal contributions. or the four Condon vectors, which contribute at negative detuning.

(3) *Manipulation of collisions:* Figure 9 demonstrates that the optical collision signal can be switched on and off by simply varying the linear polarization. This works even without resolving the interference pattern: the average intensity goes down to very small values for certain polarization directions. Similarly, Figure 9 demonstrates, how the process may be switched from one to the other possible trajectory by changing the linear polarization correspondingly. Another closely related example is provided by Figure 10. The collision pair forms an interferometer, which can be detuned arbitrarily from outside by varying the polarization. The practical applicability of these techniques may appear to be quite limited, when one looks at the systems discussed here. It is not difficult, however, to construct much more promising examples by adding *e.g.* one or more electronic states, or by going to atom - molecule systems.

(4) *Analysis of the state of the collision products, i.e. the population ratio and the alignment and orientation of the final states:* Such studies are sensitive, in the first instance, to the nonadiabatic processes, which occur on the passage of the collision pair from small to large internuclear distances (the transition from the regime of Hund's coupling cases a and b to that of the coupling cases c and e). For example at a positive detuning we populate exclusively the molecular $B^2\Sigma$ state. When we use, in addition, the techniques described in the preceding section and select a single trajectory, we prepare the collisional system with perfectly defined initial conditions immediately before it enters the nonadiabatic coupling region. The investigation of the electronic state after the collison then provides an ideal tool for the study of the nonadiabatic process. Experiments of this type have been reported so far only in a preliminary form [32]. We expect them to be among the most important applications of the new techniques in the future. When two or more trajectories are allowed to contribute to the signal, the polarization properties of the final states are the result of the nonadiabatic couplings as well as of the details of their interferences. This is illustrated by the regular structures in Figures 11, 12, 13. Complicated effects can arise in this way, as, for instance, the transfer of orientation: The orientation of the final state is expected to be different for excitation with left and right circularly polarized light. Effects like this certainly provide an extremely sensitive tool for the investigation of both the potential curves and the nonadiabatic couplings.

## Appendix A: Matrix elements in the molecular channel basis

For the matrix elements of the electronic part of the Hamiltonian in the molecular channel basis one obtains

$$< n'| < \mathcal{J}'M'l'J'|H_{\rm el}+V_{\rm so}|\mathcal{J}MlJ> |n> = \delta_{n'n}\delta_{\mathcal{J}'\mathcal{J}}\delta_{M'M}\frac{[(2l'+1)(2l+1)]^{1/2}}{2\mathcal{J}+1} \times\sum_{\Omega} C(J'l'\mathcal{J};\Omega 0\Omega)\, C(Jl\mathcal{J};\Omega 0\Omega) <J'\Omega|H_{\rm el}+V_{\rm so}|J\Omega>. \quad (37)$$

$H_{\rm el}$ and $V_{\rm so}$ are diagonal in $\Omega$ and further $V_{\rm so}$ is assumed here to be approximatively diagonal also in $J$

$$< J'\Omega|H_{\rm el}|J\Omega > = \sum_{\Lambda} C(LSJ;\Lambda\Sigma\Omega)\, C(LSJ';\Lambda\Sigma\Omega)\, V_{|\Lambda|}(R) \quad (38)$$

$$< J'\Omega|V_{\rm so}|J\Omega > \sim \delta_{JJ'}\frac{g}{2}\,[J(J+1)-L(L+1)-S(S+1)]. \quad (39)$$

With relations like $a|n>=\sqrt{n_\omega}|n-1>$ the radiative coupling term takes the form

$$< n'| < \mathcal{J}'M'l'J'|V_{\rm rad}|\mathcal{J}MlJ> |n> = \delta_{n'n-1}C(\mathcal{J}1\mathcal{J}';MqM') < \mathcal{J}'l'J'||V_{\rm rad}||\mathcal{J}lJ > \quad (40)$$

$$< \mathcal{J}'l'J'||V_{\rm rad}||\mathcal{J}lJ > = \frac{e}{m_{\rm e}}\left(\frac{2\pi\hbar n_\omega}{\omega V}\right)^{1/2}\frac{[(2l'+1)(2l+1)]^{1/2}}{2\mathcal{J}'+1} \times\sum_{\Omega\sigma} C(J'l'\mathcal{J}';\Omega 0\Omega)\, C(Jl\mathcal{J};\Omega 0\Omega) \times C(\mathcal{J}1\mathcal{J}';\Omega\sigma\Omega') < J'\Omega'|p_\sigma|J\Omega > . \quad (41)$$

As well known the momentum coupling in equation (40) is equivalent to the more standard expression in terms of a dipole coupling

$$\frac{e}{m_{\rm e}}(2\pi\hbar n_\omega/\omega V)^{1/2}p_\sigma = (2\pi\hbar\omega n_\omega/V)^{1/2}(er_\sigma) = (2\pi I_\omega/c)^{1/2}\mu_\sigma = E\,\mu_\sigma/2 \quad (42)$$

where the $\mu_\sigma$ are the dipole moments of the molecular transitions and $I_\omega=\hbar\omega n_\omega c/V$ and $E$ are the laser intensity and the corresponding field amplitude.

## Appendix B: Atomic dressed-state basis at large internuclear separations

The interaction $V_{\rm rad}$ remains finite for optical collisions in the region of asymptotic internuclear separations and the free-atom states are no longer eigenstates of the asymptotic limit of the Hamiltonian of equation (2). The scattering matrices are therefore defined for transitions among the atomic "dressed states". For large internuclear separations the transition dipole becomes $\Omega$- und $R$-independent and the radiative coupling is [33]

$$< \mathcal{J}'l'J'||V_{\rm rad}||\mathcal{J}lJ > = (-)^{\mathcal{J}'+J-1-l}\{(2\mathcal{J}+1)(2J'+1)\}^{1/2} \times W(J'J\mathcal{J}'\mathcal{J};1l) < J'||V_{\rm rad}||J > \delta_{ll'} \quad (43)$$

with

$$< J'||V_{\rm rad}||J >= (-)^{J'+L-1-S}\{(2J+1)(2L'+1)\}^{1/2} \times W(L'LJ'J;1S)< L'||V_{\rm rad}||L > . \quad (44)$$

Therefore the channel functions formed with atomic "dressed states" become at large $R$ diagonal in $l$, but not in $\mathcal{J}$, $M$, $J$ and $n$ and will be denoted by $|\alpha l>$ with

$$\{\frac{\mathbf{l}^2}{2mR^2}+H_{\rm el}+V_{\rm so}+H_{\rm ph}+V_{\rm rad}\}|\alpha l>=\epsilon_{\alpha l}|\alpha l> \quad (45)$$

In the low-field regime it is possible to represent the asymptotic dressed state channel functions using first-order perturbation theory as

$$|\alpha l>= |\mathcal{J}MlJn> + \frac{< \mathcal{J}'M'lJ'n-1|V_{\rm rad}|\mathcal{J}MlJn>}{\epsilon_J-\epsilon_{J'}+\hbar\omega}|\mathcal{J}'M'lJ'n-1>$$

$$|\alpha' l>= |\mathcal{J}'M'lJ'n'> + \frac{< \mathcal{J}MlJn'+1|V_{\rm rad}|\mathcal{J}'M'lJ'n'>}{\epsilon_{J'}-\epsilon_J-\hbar\omega}|\mathcal{J}MlJn'+1> . \quad (46)$$

The energies $\epsilon_{\alpha l}$ are unaffected up to second-order in $V_{\rm rad}$, *e.g.*

$$\epsilon_{\alpha l}=\epsilon_J+\frac{l(l+1)}{2mR^2}+n\hbar\omega \quad (47)$$

The atomic "dressed states" defined by equation (46) therefore are arbitrarily close to the unperturbed states and $\alpha$ may then as well replaced by the quantum numbers $\mathcal{J}MJnq$. The $q$ and $M$ dependencies separate by

$$|\alpha l>=|\mathcal{J}MlJn> +\delta_{nn'\pm 1}C(\mathcal{J}1\mathcal{J}';MqM') \times\frac{< \mathcal{J}'lJ'||V_{\rm rad}||\mathcal{J}lJ >}{\epsilon_J-\epsilon_{J'}+(n-n')\hbar\omega}|\mathcal{J}'lJ'M'n'> . \quad (48)$$

Due to the asymptotic degeneracy in $\mathcal{J}$ a diagonalization of equation (45) will in general not lead to the eigenvectors of equation (46) but rather result in some linear combination with ill-defined $\mathcal{J}$. The effect is treated by a basis transformation to the standard atomic "dressed states" and calculation of the $S$-matrix in this basis. From then one no further distinction is necessary between dressed and undressed channels, since any corrections are of higher order in the field. For the $S$-matrix determination the procedure is however essential since otherwise a unique result cannot be obtained and the $S$-matrices show oscillatory behaviour in $R$ similar to Rabi oscillations.

## References


1. W. Behmenburg, Phys. Scripta **36**, 300 (1987).
2. K. Burnett, Phys. Rep. **118**, 339 (1985).
3. W. Behmenburg, A. Makonnen, A. Kaiser, F. Rebentrost, V. Staemmler, M. Jungen, G. Peach, A. Devdariani, S. Tserkovnyi, A. Zagrebin, E. Czuchaj, J. Phys. B **29**, 3891 (1996).
4. K. Burnett, J. Cooper, Phys. Rev. A **22**, 2027, 2044 (1980).
5. G. Nienhuis, J. Phys. B **16**, 1 (1983).
6. F. Schuller, F. Rebentrost, Z. Phys. D **37**, 197 (1996).
7. L.R. Kundkhar, A. Zewail, Ann. Rev. Phys. Chem. **41**, 15 (1990).
8. A. Zewail, in *Femtochemistry. Ultrafast Dynamics of the Chemical Bond* (World Science, Singapore, 1994).
9. J. Manz, L. Wöste, in *Femtosecond Chemistry* (Verlag Chemie, Weinheim, 1995).
10. M. Motzkus, S. Pedersen, A. Zewail, J. Phys. Chem. A **100**, 5620 (1996).
11. F. Rebentrost, R. Best, W. Behmenburg, J. Phys. B **20**, 2627 (1987).
12. L.L. Vahala, P.S. Julienne, M.D. Havey, Phys. Rev. A **34**, 1856 (1986).
13. W. Behmenburg, A. Ermers, F. Rebentrost, Z. Phys. D **18**, 93 (1991).
14. I.M. Bell, C.J.K. Quayle, K. Burnett, D.M. Segal, Phys. Rev. A **47**, 3128 (1993).
15. S.Y. Ni, W. Goetz, H.A.J. Meijer, N. Andersen, Z. Phys. D **38**, 303 (1996).
16. D.A. Olsgaard, R.A. Lasell, M.D. Havey, A. Sieradzan, Phys. Rev. A **48**, 1987 (1993).
17. J. Grosser, D. Gundelfinger, A. Maetzing, W. Behmenburg, J. Phys. B **27**, L367 (1994).
18. J. Grosser, D. Hohmeier, S. Klose, J. Phys. B **29**, 266 (1996).
19. E.L. Lewis, M. Harris, W.J. Alford, J. Cooper, K. Burnett, J. Phys. B **16**, 553 (1983).
20. M.S. Child, in *Molecular Collision Theory* (Academic Press, London, 1974).
21. E.E. Nikitin, Ya. Umanskii, in *Theory of Slow Electronic Collisions* (Springer, Berlin, 1984).
22. K.C. Kulander, F. Rebentrost, J. Chem. Phys. **80**, 5623 (1984).
23. J. Grosser, A.E. deVries, Chem. Phys. **10**, 229 (1975).
24. I.V. Hertel, H. Schmidt, A. Bähring, E. Meyer, Rep. Prog. Phys. **48**, 375 (1985).
25. J. Grosser, Comm. At. Mol. Phys. **21**, 107 (1988); Z. Phys. D **3**, 39 (1986).
26. R.J. Bieniek, P.S. Julienne, F. Rebentrost, J. Phys. B **24**, 5103 (1991).
27. R. Brühl, J. Kapetanakis, D. Zimmermann, J. Chem. Phys. **94**, 5865 (1991).
28. R. Düren, E. Hasselbrink, J. Chem. Phys. **89**, 2822 (1988).
29. J. Grosser, O. Hoffmann, S. Klose, F. Rebentrost, Europhys. Lett. **39**, 147 (1997).
30. J. Grosser, O. Hoffmann, C. Rakete, F. Rebentrost, J. Phys. Chem. A **101**, 7627 (1997).
31. M.D. Havey, F.T. Delahanty, L.L. Vahala, G.E. Copeland, Phys. Rev. A **34**, 2758 (1986).
32. J. Grosser, O. Hoffmann, S. Klose, in *Spectral Line Shapes Vol.9, 13. Int. Conf. on Spectral Line Shapes, Firenze, 1996*, edited by M. Zoppi, L. Ulivi (AIP Conference Proceedings, vol. 386, 1997), p. 181.
33. D.M. Brink, G.R. Satchler, in *Angular Momentum* (Oxford 1986).